Generating high-harmonic array beams

Cite as: APL Photon. 10, 026109 (2025); doi: 10.1063/5.0240124
Submitted: 24 September 2024 • Accepted: 22 January 2025 •
Published Online: 13 February 2025

Andra Naresh Kumar Reddy,[1,2,3,a)] Helmut Zacharias,[4] Hasan Yilmaz,[5] Vyacheslav V. Kim,[6] Victor Kärcher,[4] Vijayakumar Anand,[7,8] and Rashid A. Ganeev[1,6,9,10]

AFFILIATIONS

[1]Laboratory of Nonlinear Optics, Institute of Astronomy, University of Latvia, Jelgavas 3, LV-1004 Riga, Latvia
[2]Quantlight & High harmonics Lab, Door No. 304, PGR Crest, Survey No. 30/P, Street No. 16, Nalanda Nagar, Hyderguda, Hyderabad 500048, Telangana, India
[3]Materials Research Center, College of Arts and Science, American University of Sharjah, Sharjah 26666, United Arab Emirates
[4]Department of Physics and Center for Soft Nanoscience (SoN), University of Münster, 48149 Münster, Germany
[5]Institute of Materials Science and Nanotechnology, National Nanotechnology Research Center (UNAM), Bilkent University, 06800 Ankara, Turkey
[6]Institute of Fundamental and Applied Research, TIIAME National Research University, Kori Niyoziy 39, Tashkent 100000, Uzbekistan
[7]Institute of Physics, University of Tartu, W. Ostwaldi 1, 50411 Tartu, Estonia
[8]Optical Sciences Center and ARC Training Centre in Surface Engineering for Advanced Materials (SEAM), School of Science, Computing and Engineering Technologies, Optical Sciences Center, Swinburne University of Technology, Hawthorn, Melbourne, VIC 3122, Australia
[9]Western Caspian University, Istiglaliyyat Street 31, Baku AZ1001, Azerbaijan
[10]Department of Optics and Spectroscopy, Voronezh State University, Voronezh 394006, Russia

[a)]**Author to whom correspondence should be addressed:** naarereddy@gmail.com

ABSTRACT

The demand for spatially structured ultrashort beams at shorter wavelengths is high, and their adaptability in potential applications such as imaging, metrology, and attosecond science is undeniable. In this work, we present the generation of high-harmonic array beams. We utilize ultrashort structured array beams in the near-infrared wavelength as the pump source to reliably generate extreme-ultraviolet array beams at the tenth harmonic of the pump wavelength. The pump array beams showed shape-invariant free space propagation and exhibited a self-healing ability against adverse spatial effects introduced by aberrations. Moreover, we found that the spatial profile of these array beams remained unchanged for any polarization state, a unique feature that enhances their versatility. The interaction of shape-invariant array beams with an argon gas jet in a two-color pump configuration generated high harmonics consisting of both weak odd and even orders, a suppression of odd harmonics from the 13^{th} to the 17^{th} order when driven by two-color laser fields, but a strong 10^{th} order harmonic appeared in the extreme-ultraviolet. This 10^{th} harmonic unveiled a spatial distribution, including a unique string structure that is a hallmark of array beams. This extreme nonlinear optical process of structured high-harmonic generation is a significant advancement that offers a new degree of freedom for generating diverse structured harmonics in extreme ultraviolet and soft x-ray regimes.

I. INTRODUCTION

The development of laser systems, spatial light modulators, and diffractive elements that shape high-power laser pulses with high repetition rates has greatly expanded the applications of laser–matter interactions. These include vortex beams carrying twisted light with phase rotation around the propagation axis that preserves orbital angular momentum (OAM),[1,2] vector beams with polarization singularities,[3–5] vector-vortex beams,[6,7] Laguerre–Gaussian beams,[8,9] and spatiotemporal optical vortices.[7,10–13] Those

structured beams are advantageous in various applications, such as optical communications, where OAM offers another degree of freedom in modulation and multiplexing that increases transmission capacity and density.[14,15] OAM can also be applied to trap micro-particles and move them orbitally in optical tweezers.[16–19] Structured beams are beneficial in nanoscale fabrication and surface modification in semiconductor materials, polymers, and silica glass,[20–22,26,27] as well as high-order harmonic generation (HHG) in rare gases[23–25] and 3-D imaging.[28,29]

In particular, the investigation of optical beams with quasi-invariant and non-diffracting nature has grown rapidly in the past several years, and their unique landscapes allow for exploring potential benefits in light–matter interaction experiments. In this context, the Airy beam has made significant advancements as it has a special property of propagating in a parabolic path, demonstrating self-acceleration without any additional optics that could be useful in micromachining or optical welding of surfaces at higher intensities. It is a non-diffracting beam showing a self-healing nature against obstructions.[30] These beams with radial symmetry are considered circular Airy beams and are well-known for abrupt autofocusing properties, which makes them strong candidates in the optical trapping of microparticles.[31,32] Bessel beams are among the most important non-diffracting beams with propagation-invariant properties shown during free-space propagation,[33] which are highly desirable for obtaining concrete benefits in dicing and modification of transparent materials,[34,35] optical manipulation,[36] and 3D fluorescence imaging.[37] However, their non-diffracting propagation length is limited to the wavelength level.[38] Before the evolution of Bessel beams,[33] achieving this important property for laser beams was a significant challenge due to diffraction, which is the inherent wave nature of light. However, by effectively tackling these challenges through efficient beam shaping techniques, we can preserve the beam shape while increasing only the beam size during propagation in free space.

Different approaches have been developed to generate structured light beams with unique propagation characteristics, including direct and external beam shaping techniques. Recently, an approach for generating arbitrary shape-invariant structured array beams was reported by devising a suitable far-field phase attached to the initial field using an external beam-shaping mechanism realized by spatial light modulators (SLMs).[39] However, a direct approach for generating structured beams with high efficiency in output, carrying high purity,[40] and generating different structured modes is very challenging with this approach. The significance of external beam-shaping was demonstrated in various applications in which SLMs,[17,20–22,28,31,32,38,41,42] digital mirror devices (DMDs),[43–45] and diffractive optical elements (DOEs), either lithography-produced or femtosecond laser written, were employed.[19,20,23–25,34–36,45] In particular, SLMs and DMDs are not ideal candidates for experimental schemes involving high-power lasers, particularly when pulse energies at millijoule levels or higher are employed. Moreover, these dynamic digital devices are subject to low-diffraction efficiency outputs, and their liquid-crystal screens respond to a certain polarization of the incident light beam. In industrial and space applications such as ultra-short laser welding and drilling and satellite laser ranging and tracking, there is a high possibility of pixel damage to the liquid crystal display, which makes them economically inefficient to employ. Similar arguments hold for the generation of extreme ultraviolet beams via high-harmonic generation in gas media.

In this paper, we demonstrate high-harmonic generation using structured array beams with shape-invariant or propagation-invariant characteristics. First, array beams are generated and characterized at near-infrared wavelengths, presented as the pump source. In this context, a binary-phase DOE is employed, the phase profile of which is etched into a pure fused silica substrate with a high laser damage threshold. The generated ultrashort shape-invariant array beams have unique propagation characteristics, making them promising candidates for beneficial applications and laser–matter interaction experiments. Therefore, the propagation characteristics of these array beams are evaluated at different distances in free space and compared with the Gaussian beams at the same distances. The resulting array beams with shape-invariant features have shown a self-healing ability against deformation induced by astigmatism of optical elements in the beam path. In addition, ultrashort array beams are produced for diverse wavelengths whose performance is substantially competitive relative to the array beams demonstrated for the manufacturing wavelength (λ = 1064 nm) of the binary-phase DOE. The array beams with different polarizations in the focal region are shown to have similar intensities and have proven insensitive to changes in the polarization state. The resultant intensity distribution of the generated array beams is spread over four quadrants in the x and y directions, thereby mimicking the intensity distribution of Airy array beams with rectangular symmetry comprising four individual off-axis Airy beams.[46,47] However, the generated ultrashort array beams demonstrated in this paperwork do not exhibit the properties of Airy array beams, such as accelerating along the curved parabolic trajectory while being robust to perturbations, and they can also circumvent obstacles.[47]

Exploring the consequences of pump array beams in light–matter interaction experiments, particularly in high-power nonlinear laser interaction with matter (e.g., HHG), is a challenging and highly desired process that has not yet been reported. We demonstrate the generation of XUV array beams by HHG in argon gas. The uniqueness of this investigation is a two-color pump [fundamental and second harmonic emissions ($\omega + 2\omega$)] to generate high-order harmonics using the focused pump array beams, thus extending commonly used HHG in argon driven by Gaussian laser beams. For the strongly enhanced 10^{th} harmonic (10H) in this two-color pump (TCP) configuration, we observe that the spatial features of pump array beams are maintained and preserved for two different locations of the DOE in the input beam. This constitutes a significant advancement for the generation of spatially structured XUV harmonics. Along with the intense 10H, we detected weak odd and even orders and a clear suppression of higher odd-order harmonics (13H–17H). However, for a spatially structured fundamental pump beam, the intensity at the focal spot can be optimized such that odd-order XUV harmonics with spatial features of pump array beams appear. This proof-of-principle demonstration opens new avenues for implementing structured array beams in various applications, such as high-harmonic radiation in gases and plasma media, optical tweezers, optical trapping, high-resolution XUV microscopy, XUV lithography, coherent diffractive imaging, and optical communication.

II. GENERATION AND DESCRIPTION OF ARRAY BEAMS

A. Fabrication of the DOE

The pump array beams are generated via a UV transparent DOE, which possesses alternating regions of 0 and π relative phase difference. The spatial arrangement of these regions [Fig. 1(c)] determines the internal structure of array beams. The relative phase of the DOE is fabricated by a direct laser writing lithography process followed by dry plasma etching (reactive ion etching) to produce a fine diffractive surface structure into a UV-grade fused silica substrate of 3 mm thickness. A photoresist (Merck, AZ4533) is used to protect areas that should not be etched in this process. The etching depth amounted to 2 μm, and steep side walls ensure a high contrast in the array beam. The surface quality of the 25.4 mm UV-fused silica substrate selected for DOE manufacturing was 60–40 s/d (scratch number followed by dig number). After fabrication, the substrate was cleaned with an organic solvent and plasma ashing the photoresist, enabling a quality and high damage threshold surface to facilitate the use of DOE in high-power laser experiments. The thickness difference between adjacent regions, or the height difference for the phase difference of π in the fabricated DOE, is evaluated as $d = \frac{\lambda}{[2(n_1 - n_2)]}$, where n_1 is the refractive index of fused silica ($n_1 \sim 1.457$), n_2 is the refractive index of the ambient environment (which here is air and, thus, $n_2 = 1$), and λ is the manufacturing wavelength, in this case, λ = 1064 nm.[48] Therefore, the height change of adjacent regions differed by π phase amounts to $d = 1164$ nm. The parametric study of the writing laser beam in the lithography process includes

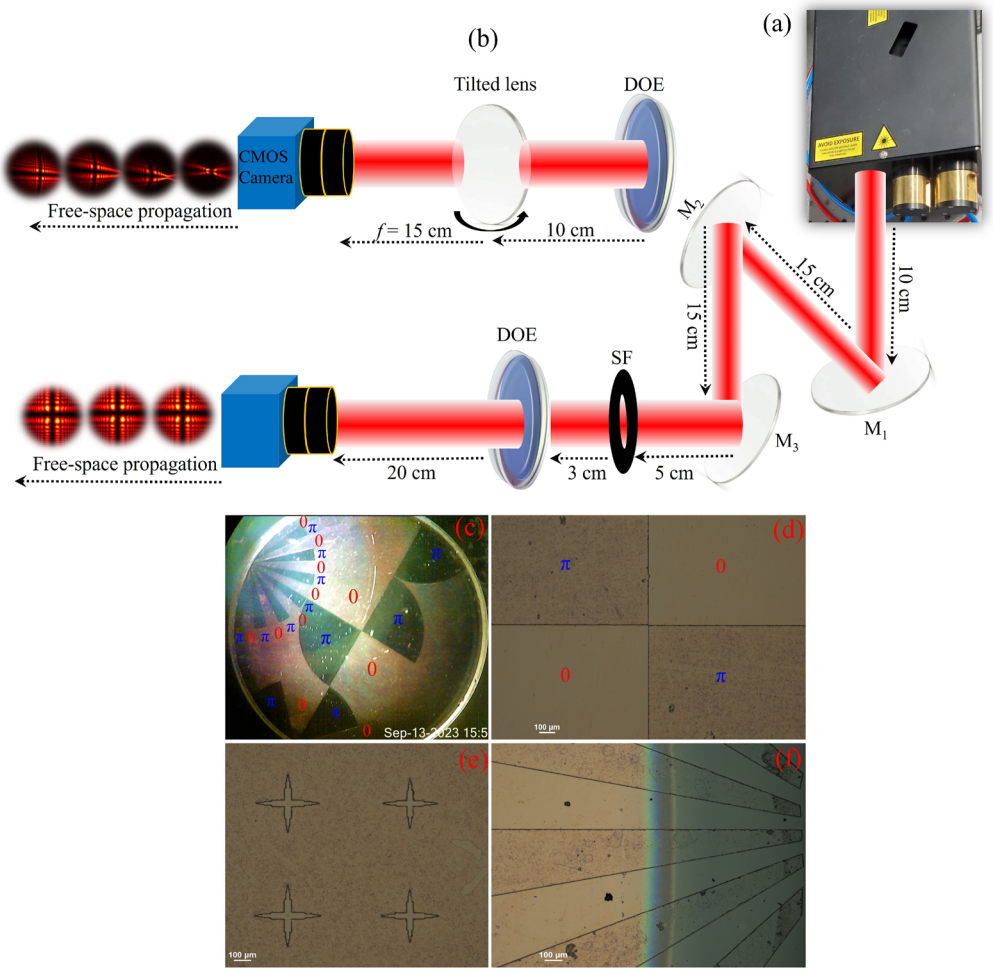

FIG. 1. (a) Experimental arrangement for generating and characterizing shape-invariant ultra-short array beams. Femtosecond laser of tunable wavelength; M_1, M_2, and M_3 are the reflective mirrors; SF- spatial filter for cleaning the Gaussian input beam; DOE- diffractive optical element, which is a binary phase element; and CMOS camera. (b) The optical arrangement with a tilted lens is located 10 cm from the DOE position, and the CMOS camera is placed in the focal plane of the plano–convex lens (f = 15 cm). The optical microscope image of the manufactured diffractive phase element consists of sectors indicating regions with 0 and π phase imprint. (c)–(f) Microscopy images of the central part, the region of cross-petals in the central part, and the region of triangles located next to the central part of the DOE-phase structure. The scale bars in (d)–(f) are 100 μm.

pulse energy and repetition rate, and the time interval between two consecutive writing laser pulse shots optimizes the height disparity between adjacent regions in the fabricated binary-phase DOE, which is expected to be around the calculated d (~1164 nm).

B. Experimental arrangements

A schematic of the experimental arrangement for generating and propagating ultra-short shape-invariant array beams is shown in Fig. 1(a). The experimental setup employs a tunable femtosecond laser source (Light Conversion, Orpheus-HP + Pharos PH2, λ ~ 200–2100 nm, pulse duration 150 fs, 500 Hz repetition rate, 10 W output power). It produces an output beam with a Gaussian profile, whose wavelength was tuned to 1064 nm. The laser beam is linearly polarized (horizontal) and then expanded after passing through the arrangement of the reflecting mirrors (M_1, M_2, and M_3), as shown in Fig. 1. The expanded Gaussian beam passes through a spatial filter (SF) to suppress high-frequency spatial oscillations. The resultant Gaussian beam with an improved intensity profile impinges normally onto the binary-phase DOE that shapes the amplitude and phase of the Gaussian input beam corresponding to its imprinted phase structure, resulting in the output beam presented as ultrashort array beams.

The beam shaped by the DOE propagates in free space. The propagation characteristics of the generated ultra-short array beams were evaluated at different distances up to 40 cm from the DOE in free space by a CMOS camera (Ximea, MQ013MG-E2, a pixel size of 5.3 μm mounted on a motorized translation stage) [Fig. 1(a)]. Figure 1(b) shows a slightly modified experimental arrangement where a tilted lens introduces artificial astigmatism into the array beams.

The diffractive phase structure developed on the surface of the DOE [Fig. 1(c)] modifies the transverse profile of the Gaussian beam due to the variation in optical properties for adjacent regions defined by the phase change of π. To better illustrate the DOE, surface microscopy images provided details of phase variation over different regions in the phase structure etched into the fused silica substrate, as shown in Figs. 1(d)–1(f). The central part of the DOE phase structure consists of four sectors, and the cross-petals arrangement shown in the π phase zone together plays a decisive role in producing the output array structure, which is distributed in the x and y directions separated by dark channels.

The dimension and peculiarity of the structured array light field produced by the DOE depend upon the number of sectors or triangles (N) and other unique arrangements of the phase structure. The spatial features and the variations of the light field intensity of the generated structured-array beam change with the number of phase zones, particularly phase zones positioned in the DOE center and other phase zones configured in the DOE phase structure. The increase in the number of sectors with specific widths in the middle part leads to increased divisions in the resulting array beam field distributed in the x and y directions.[48,49] However, the precise dependence needs to be clarified by further investigation into such diffractive optical elements. Recently, the fabrication of high-quality DOE as a structured grating was reported to be more efficient than binary elements for shaping XUV harmonics.[50] Notice that the efficiency differs with the nature of structured light that the DOE generates for driving structured XUV harmonics. The binary-phase DOE was meticulously chosen for the present work as the DOE is efficient and has proven to be an easy attempt to generate pump array beams as a driving field for generating structured XUV harmonics with unique landscapes. It is also realized that the DOE with robust design employed for generating ultrashort array beams or shaped laser beams shows a consistent tolerance for operational errors, such as misalignment to the incoming beam, input beam quality, and shape that deviated from the fundamental mode of the Gaussian laser beam.[51–54]

C. Characteristics: free-space propagation, spectral effect, and polarization

We first determined the beam properties of propagating Gaussian beams at different z-positions in free space in order to compare those with the propagation features of the array beams. Please note that in the present experimental arrangement, the Gaussian beam from the laser source first traveled an optical distance of around 50 cm to reach the DOE position, and then the intensity profile was measured for an additional 20–40 cm of propagation distance towards the camera. As expected, the Gaussian beam size slightly increased with the propagation distance [Fig. 2(a)]. Evaluating beam sizes at different distances in free space yields beam diameters of 3.64 mm (FWHM) at z = 20 cm, 3.95 mm at z = 30 cm, and 4.30 mm at z = 40 cm, thus a beam divergence of 3.3 mrad. Generally, diffraction occurs when a light beam propagates in free space, and subsequently, due to the diffraction, the beam diverges. For a Gaussian beam with a long Rayleigh range in free space, the beam divergence can be estimated as $\theta = \frac{\lambda}{\pi w_0}$. The beam divergence is thus directly proportional to the wavelength λ and inversely proportional to the beam waist (w_0).[54] The corresponding non-diffracting length or depth of focus is inversely proportional to the beam divergence (θ). The most common way to diminish the negative influence of beam divergence is to employ beam expanders that regulate the position of the beam waist, thus improving the experimental arrangement. Another alternative approach is using a Fresnel plate that exclusively focuses the light at a single point.[55]

These results are then compared with the intensity profiles obtained by inserting the DOE into the beam path. Figure 2(b) depicts the results of ultrashort array beams measured downstream from the binary phase DOE. The generated array beams with multiple intensity lobes are symmetrically arranged in four quadrants. Evidently, the resulting beam structure is conserved for propagation in free space of at least 20 cm, and the array beam was thus invariant in its spatial structure. The corresponding cross-sectional intensity profiles are included in the right column of Fig. 2(b). In each quadrant, the generated array beam consists of a localized mainlobe accompanied by sidelobes in the x and y directions. The intensities of sidelobes decrease with increasing distance from the center. For a better understanding of propagation features in the cross-sectional intensity profiles, black-dashed lines are aligned at the peak positions of the mainlobes of array beams illustrated in the right column of Fig. 2(b) and are separated by a distance D.

The generated structured array beam size increases with the propagation distance but preserves the shape of the array beam. This prominent feature is observed for the intensity distributions detected at z = 20 cm, z = 30 cm, and z = 40 cm and included in the right column of Fig. 2(b). The results show that the distance D between

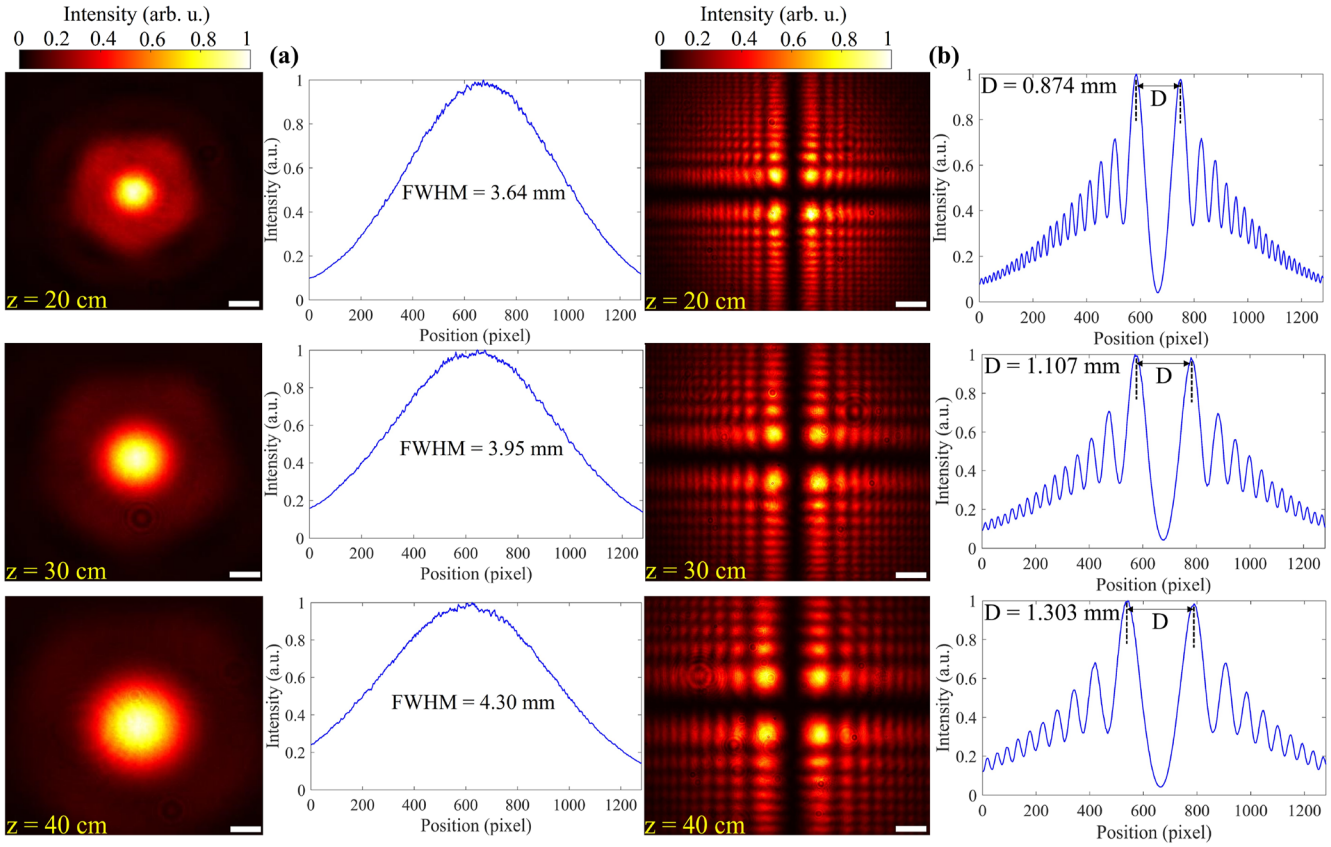

FIG. 2. Propagation of beams in free space: (a) Gaussian beam intensity profiles at various propagation distances z = 20 to 40 cm are shown in the left column, together with the corresponding cross-sectional intensity profiles, which are shown in the right column; and (b) ultrashort array beam intensity profiles at various propagation distances z = 20 to 40 cm are shown in the left column, and the corresponding cross-sectional intensity profiles are shown in the right column. D represents the distance between the centers of the mainlobes in the intensity profiles measured at different distances of free-space propagation. White bars in (a) and (b) represent the scale of ~0.65 mm.

the mainlobes of the intensity distributions of the array beam at z = 20 cm is 0.874 mm, increasing to 1.107 mm and 1.303 mm for distances z = 30 cm and z = 40 cm, respectively. This corresponds to a divergence of 2.14 mrad. The increase in array beam size is exemplified by widened mainlobes and sidelobes in the resultant intensity distributions shown in Fig. 2(b). Despite this, the shape of the array beam is preserved and remains unchanged. Please note that the resultant ultrashort array beam consists of a pattern of spots rather than a single spot, and the area illuminated by the array laser beam is larger than the Gaussian laser beam. The beam divergence of the generated structured laser array beam is defined by evaluating the ratio of the difference between the final distance (D_f) and the initial distance (D_i) measured for the mainlobes as a function of z and the propagated distance (δz) between the initial and final planes in free space. The experimental uncertainty for spacing between the diffraction lobes (D) is evaluated using the number of datasets that are obtained at each propagation distance, and the standard deviation of those datasets was calculated as 0.00223 mm, 0.00273 mm, and 0.00466 mm for D values at different propagation distances. In other words, the standard deviation is 2.23 μm, 2.73 μm, and 4.66 μm for the datasets measured at z = 20 cm, 30 cm, and 40 cm, respectively. Please note that the camera employed to record those experimental datasets has a pixel size of 5.3 μm.

Generally, the output array beams downstream of the binary-phase DOE consist of an array of intensity distributions positioned into four symmetric quadrants. The four-lobe structures show the same intensity and are separated from each other by the same distance in the x and y directions. In each quadrant, the resultant intensity distribution consists of the mainlobe with high intensity and relatively weaker paraxial intensities. The width of lobes with respect to the *x*-coordinate increases with propagation in the z-direction. Overall, the generated structured array beam preserves its intrinsic structure, i.e., its transverse profile remains invariant during propagation regardless of the increase in the size of the array beam. In the present work, this shape-invariant structure of the ultra-short array beam is perfectly preserved up to 40 cm from the DOE position. Please note that the shape-invariant features of well-known Airy or Bessel beams are preserved over longer distances than those of structured array beams investigated in the present work. For longer propagation distances in free space, the size of the shape-invariant structured array beam increases more. Thus, the

total laser array pattern can be captured with a camera mounted on an XYZ translation stage, allowing for consecutive measurements with a sensor size of 6.8 × 5.4 mm^2.

We further experimentally investigated the self-healing ability of structured-array beams from adverse effects introduced by aberrations. A classical spherical lens adds a quadratic phase to the incoming beam while focusing. In order to introduce astigmatism into the array beam, a spherical lens with a focal length of f = 15 cm is mounted on the rotating module, positioned at 10 cm behind the DOE, and tilted by an angle α with respect to the y-axis. In spherical lens approximation,[56] a small tilt effect is induced, equivalent to the larger phase delay in the lens plane (x, z), resulting in a smaller focal length f_1 on the horizontal axis (x), $f_1 = f\cos\alpha$, and a larger focal length f_2 on the vertical axis (y): $f_2 = f\,(\cos\alpha)^{-1}$. Therefore, the transmittance of a tilted spherical lens is given as $T(x,y) = \exp\left(-\frac{ikx^2}{2f_1} - \frac{iky^2}{2f_2}\right)$, where k is the wavenumber and f is the focal length of the spherical lens.[56]

The tilted spherical lens is equivalent to an arrangement of two crossed cylindrical lenses with different foci.[56] Note that tilting the spherical lens relative to the y-axis by an angle of $\alpha = 45°$, as shown in Fig. 1(b), results in an astigmatic transformation of the entire intensity profile of the structured-array beam at propagation distance z from the binary-phase DOE. The intensity profiles obtained with the titled spherical lens are illustrated in Fig. 3. At the focal position of the lens, z = 0 cm [Fig. 3(a)], we observe an aberrated intensity profile. This aberrated intensity profile shows a self-healing ability during free-space propagation, as is evidenced by the images at z = 0.5 cm [Fig. 3(b)], 1 cm [Fig. 3(c)], and 2 cm [Fig. 3(d)] behind the focal position of z = 0 cm. At the distance z = 3 cm [Fig. 3(e)], the intensity profile has almost recovered from the adverse effects introduced by the tilted lens. Further propagation of the intensity pattern from z = 3 cm to 5 cm establishes the self-healed undistorted array beam, as illustrated in Figs. 3(f) and 3(g). For longer distances, the resultant intensity pattern remains shape-invariant.

Figure 4 illustrates representative intensity profiles of ultrashort shape-invariant array beams produced for different laser wavelengths. The CMOS camera, mounted on a translation stage, is positioned at a distance of z = 20 cm from the DOE to collect the corresponding intensity profiles. The quality of the output array beams obtained at different wavelengths is relatively high despite the DOE being optimized for an input laser wavelength of λ = 1064 nm [Fig. 4(c)]. Please note that the quality of the array beam generated for the input laser with a wavelength of 900 nm [Fig. 4(b)] is higher than the input laser wavelength of 800 nm [Fig. 4(a)]. The loss in energy transfer from the input to the output of DOE increases by 5% for 800 nm laser compared to 900 nm laser. Despite variations in output beam quality and energy transfer, the performance of array beams at λ = 800 nm is highly appreciated as the shape and features of the array beam are completely preserved. We use this array beam as a pump source for driving the process of high-harmonic generation in a noble gas, as will be presented in Sec. III.

The polarization characteristics of structured-array beams can be described by the Poincaré sphere, as depicted in Fig. 5. An

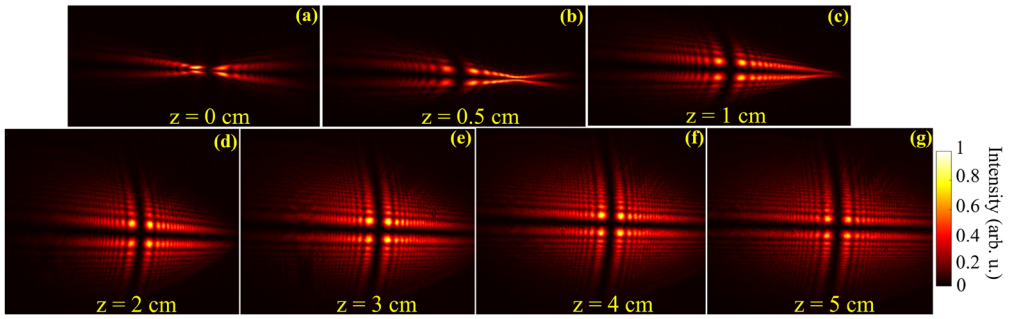

FIG. 3. Astigmatic transformation and self-healing ability of shape-invariant array beams propagating over a distance from the focal plane (z = 0) of the tilted plano–convex lens (f = 15 cm). The intensity distributions of array beams obtained through the titled lens at various propagation distances in free space: (a) z = 0 cm (focal plane); [(b)–(d)] z = 0.5 cm, 1 cm, and 2 cm; [(e)–(g)] z = 3 cm, 4 cm, 5 cm.

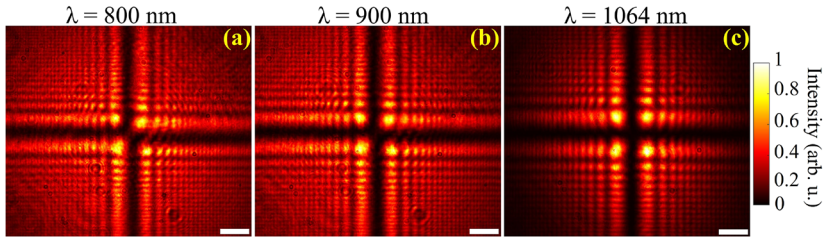

FIG. 4. Generating ultrashort array beams at different wavelengths. The DOE was manufactured for the wavelength λ = 1064 nm and is verified to generate array beams when the DOE is illuminated by Gaussian input beams of wavelengths (a) λ = 800 nm, (b) λ = 900 nm, and (c) λ = 1064 nm. White bars represent the scale of ~0.65 mm.

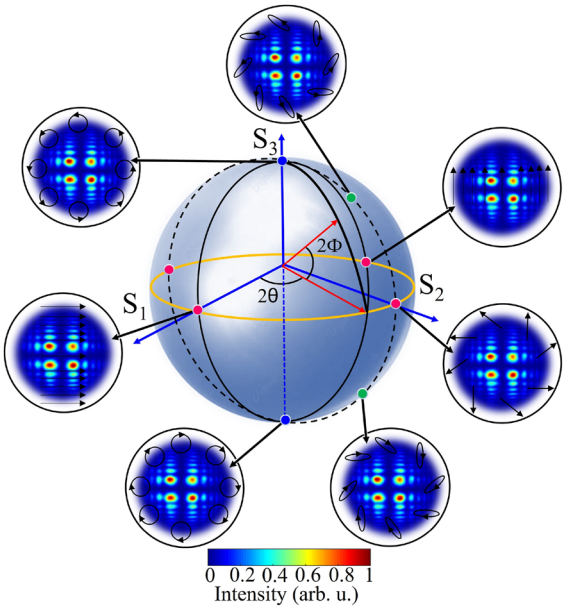

FIG. 5. Poincaré sphere representation of ultrashort shape-invariant array beams. S_1, S_2, and S_3 are the Stokes parameters of the polarization state, and 2θ and 2Φ represent the azimuthal and polar angles, respectively. The ellipticity angles are measured from the Cartesian axis S_1 and the equator. Red dots on the equator correspond to the generalized array beams that include horizontal linear and vertical linear polarized beams, blue dots at the poles indicate the circularly polarized light, and other points on the sphere represent the elliptically polarized beams.

azimuthally rotated half-wave plate adjusted the polarization of the Gaussian input beam that is incident on the quarter-wave plate positioned behind the DOE. By setting the quarter-wave plate (QWP) rotation to different angles, the DOE generates array beams via a spherical lens with different polarization states, including pure and mixed states distributed on the Poincaré sphere, where $2\Phi \in (-\pi/2, \pi/2)$ and $2\theta \in (0, 2\pi)$ denote the polar and azimuthal angles of arbitrary points.

Adjusting the QWP with its fast axis rotated to an angle of $\pm 45^\circ$ changes the polarization states that transform from the linearly polarized state of structured-array beams into left-handed and right-handed circularly polarized states. In the Poincaré representation, these polarization states are located at the poles of the sphere, indicated by blue dots located on the north $(2\theta, \pi/2)$ and south poles $(2\theta, -\pi/2)$. Other points on the Poincaré sphere represent the elliptically polarized array beams when the QWP is rotated to other angles. The red dots on the equator of the Poincaré sphere at $+S_1$ and $-S_1$ indicate the horizontal linear (0, 0) and vertical linear (π, 0) polarized array beams. Another red dot at (π/2, 0) represents the generalized linearly polarized structured-array beams. The points corresponding to elliptically polarized array beams are found at (π/2, π/4) and (π/2, −π/4), respectively, and are denoted by green dots on the Poincaré sphere. For all these polarization states described by the Poincaré sphere, the intensity of array beams remains almost constant. A change in the polarization state does not alter the propagation characteristics of array beams being shape-invariant. In short, the present DOE output does not depend on the polarization state and, therefore, can shape a Gaussian beam with any polarization state into an array beam. This study motivates us to use array beams whose intensity and spatial shape remain unaffected by a change in polarization state.

III. GENERATION OF HIGH-HARMONIC ARRAY BEAMS

The schematic of the experimental arrangement for HHG in argon employing an array beam is depicted in Fig. 6(a). The Ti:sapphire driving laser pulses at a wavelength of 800 nm exhibit a pulse duration of 60 fs, a pulse energy of 400 μJ, and a 1 kHz pulse repetition rate displayed in thick black arrows. The array beam formed by the DOE is frequency doubled in a 0.2 mm thick barium borate (BBO) crystal with a conversion efficiency of about 5%. The corresponding second harmonic radiation (SH) at λ = 400 nm interacts alongside the 800 nm radiation with the Ar gas jet in the vacuum chamber. In this process, the nonlinear conversion efficiency of the pump beam with a Gaussian profile toward the second harmonic of 800 nm emission (i.e., 400 nm radiation) is measured to be 5%. A spherical lens with f = 500 mm focused this dual color array laser field into the argon nonlinear medium. The profile of the fundamental driving laser field obtained from the DOE is shown in Fig. 4(a).

The generated harmonics and driving emission are analyzed by the XUV spectrometer featuring a flat-field variable line space grating (FFG, Hitachi, 001–0437; please refer to Fig. S1 in the supplementary material) with a 3° glancing angle of incidence and a microchannel plate (MCP) coupled with a phosphor screen. A CCD camera (Basler acA780-75gm, a pixel size of 8.3 μm) is employed to accumulate the raw images of the harmonic spectra from the MCP detector and phosphor screen. In this configuration, the orthogonally polarized two-color pump radiation was employed.[25,57] Notice that the SH conversion efficiency strongly depends on the combination of the polarization vector direction relative to the λ/2-plate rotation angle and intensity distribution. Hence, the intensity distribution of the pumping beam in the near field formed by the binary-phase DOE resulted in a structured light field distribution of fundamental and SH emissions (ω + 2ω) in the focal spot formed inside the Ar gas jet, which turned into triggering a high harmonic field along the wavefront.

The use of a two-color pump (TCP) field is a highly effective strategy for significantly enhancing harmonic output. This method not only boosts the efficiency of high-order harmonic generation but also successfully produces both even and odd harmonics. When employing a TCP, the output of odd harmonics can be increased to that of a single-color pump, and the intensities of the even harmonics are approximately equal to those of the odd harmonics. The mechanisms driving this harmonic enhancement have been explored, demonstrating the power and potential of TCP for driving this process.[58–60]

In the present approach, the polarization direction of the 800 nm laser field was linear and vertical, and that of the 400 nm field, as determined by the orientation of the phase-matched BBO crystal, was linear and horizontal. A slight rotation of the incident 800 nm polarization by a half-wave plate up to 16° from the vertical one optimized the intensity of the generated high-order harmonics in the TCP arrangement. The operating conditions remained

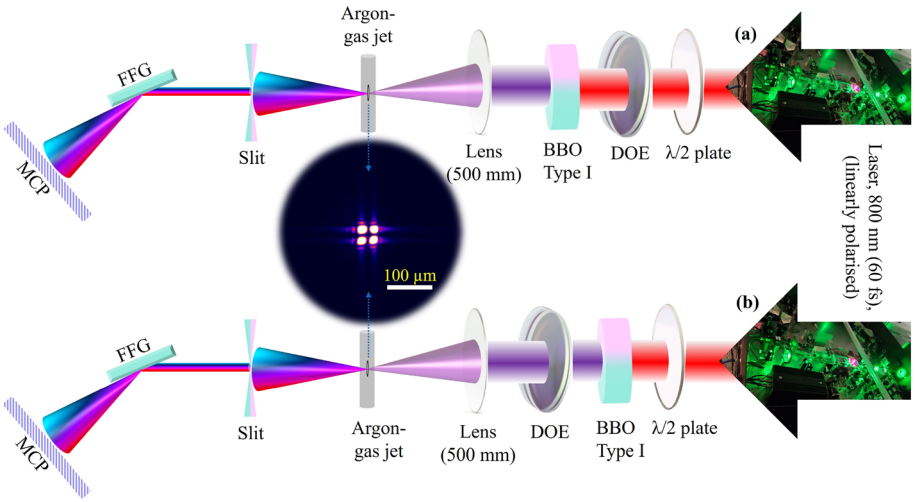

FIG. 6. (a) Schematic of the experimental arrangement in HHG using array beams. DOE (the diffractive optical element), or binary-phase plate, is irradiated by 800 nm laser radiation originating from the laser system showcased in thick black arrows; BBO (barium borate crystal) is installed before the focusing lens (lens, f = 500 mm); FFG (flat-field grating); and MCP (microchannel plate) with phosphor screen. (b) The positions of DOE and BBO are interchanged by each other, resulting in the DOE being irradiated by 400 nm laser radiation. The focal spot of the interacting laser field is shown in a circular inset marked with blue arrows.

unchanged during our experimental measurements, representing optimal conditions for forming an orthogonally polarized two-color laser field that drives the HHG process in argon gas. Please note that the polarization state of the two-color pump (800 + 400 nm) after propagation through the DOE is rather complex. It depends on the transmittance of DOE at the wavelengths of those two laser sources, as well as on the mismatch of these laser pulses due to the group velocities dispersion.

As mentioned earlier, the DOE was manufactured for a wavelength of λ = 1064 nm, but the DOE is now used at wavelength λ = 800 nm, which affects the performance, as illustrated in Fig. 4(a). Please note that the strength of high-order harmonics decreases markedly with increasing ellipticity of the driving laser field,[61] while low-order harmonics remain less affected by this factor.[62] Notably, when removing the DOE from the experimental setup, we successfully generated high-order harmonics using a vertically polarized single-color laser field (800 nm). More importantly, the intensity of the driving laser field (800 nm) at the focal plane needs to be increased after passing through the binary-phase DOE to generate high-order harmonics with distinct spatial features representing array beams at the XUV wavelengths. Therefore, we adopted the interacting laser field produced by the two-color pumping configuration instead of a single-color pump approach. This is realized by inserting the BBO crystal into the beam path. Subsequently, the two-color pump configuration is tuned and optimized to observe the HHG field with a strong 10^{th} harmonic, and the odd and even harmonic orders continue with rather weak intensities, however, with visible spatial features. Certain harmonic orders were diminished in the high-harmonic spectrum.

Figure 7(a) shows the images of odd (9H, 11H, 13H, 15H, 17H) and even (10H, 12H, 14H, 16H) harmonic signals obtained with the nonlinear interaction of two-color Gaussian driving laser pulses, in which the pump or fundamental beam polarization vector is vertical, and the SH beam polarization vector is horizontal, joining together to produce a TCP configuration.[25] We observed TCP-induced 2(2n + 1) harmonics (10H, 14H) and the appearance of 4(n + 1) harmonics (12H, 16H), which evidence a good overlap of both SH pulses and fundamental pulses (ω + 2ω) in the gaseous medium.[25]

The polarizations of odd (9H, 11H, 13H, etc.) and even 4(n + 1) (8H, 12H, 16H, etc.) harmonics in the case of TCP follow the polarization of the strongest pump (i.e., 800 nm pump) for small ratios of second harmonic and fundamental pumps. However, the 2(2n + 1) even harmonics, such as 10H, 14H, and 18H orders, follow the polarization of the 400 nm field orthogonally polarized to the fundamental (800 nm) field. From 9H to 14H [as shown in Fig. 7(a)], the XUV harmonics are observed with enhanced intensities and spatial divergence in contrast to XUV harmonics from 15H to 17H, for which the effect of the SH pump seems to be decreased. It should be noted that for 10H, the conversion efficiency for SH is high in the two-color pump configuration. The 10^{th} harmonic in the HHG field is considered as the fifth harmonic associated with the second harmonic (2ω) λ = 400 nm driving field.

Figure 7(b) corresponds to generating high harmonic array beams with an experimental arrangement, as illustrated in Fig. 6(a). This process involves illuminating the DOE with a vertically polarized 800 nm spectral component, which effectively overlaps with a horizontally polarized second harmonic (SH) spectral component from the BBO crystal in a two-color pump that interacts with argon gas. As a result, we observed high-order harmonics (9^{th} and 10^{th}) that reflected the spatial features of the segment of the laser field interacting with the gaseous medium. This experimental observation clarifies that the intensity drops at the center of the generated harmonics cannot be observed as seen in the spatial distribution of the original array laser field emitted from the binary-phase DOE [Fig. 4(a)]. However, supplying argon in a vacuum chamber via a nozzle of ~0.7 mm diameter will facilitate an effusive or molecular beam with a cone of angle 60° that can accommodate the full field of the array beam focused in the argon gas.

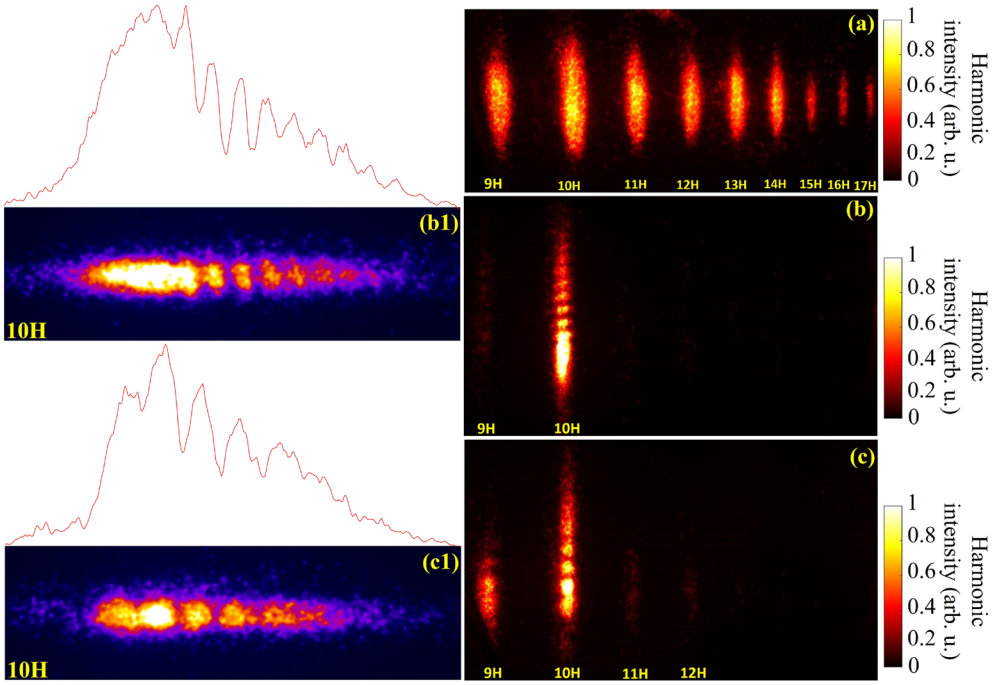

FIG. 7. (a) HHG without DOE presence in the path of the driving beam; (b) HHG using array beams formed by the experimental scheme shown in Fig. 6(a); and (c) HHG using array beams formed by the experimental scheme shown in Fig. 6(b). High-harmonic array beam (10H) when the DOE illuminated by (b1) fundamental radiation (800 nm) from two-color pump (c1) SH radiation (400 nm) from two-color pump configuration. In both cases, the 400 nm radiation was horizontally polarized, and that of the 800 nm radiation was predominantly vertically polarized. The intensity of the generated high-order harmonics in the TCP arrangement was optimized by slightly adjusting the 800 nm polarization by a half-wave plate.

By positioning the DOE before the frequency doubling BBO crystal [as shown in Fig. 6(a)], the overlapping efficiency of the SH pump in TCP configuration is significantly weaker, leading to the disappearance of odd and even harmonics except for the 10^{th} harmonic, which appeared due to TCP-induced enhancement. In this process, a portion of the structured array beam ($\omega + 2\omega$) interacts with the gas medium to generate TCP-induced $2(2n + 1)$ harmonic. The spatial profile across the generated high harmonic beam is a vertical structure attributed to TCP conditions that closely resemble features of a portion of the shape-invariant array beams. For the intensity profile corresponding to the 10H, one can observe the strong bright area generated by the mainlobe, followed by dark and secondary bright areas generated by the sidelobes of the array beam. The distance between the Ar gas jet and the MCP position in the experimental arrangement shown in Fig. 6 is more than one meter. Even after propagating such a distance, the wavefront of the 10^{th} harmonic still preserves the spatial shape of the structure in the generating array beam obtained from the DOE, which is a significant advancement in generating high harmonics with unique spatial features. Note that 9H also appeared but only with a very weak intensity (see Fig. S3 in the supplementary material).

In this process, the XUV harmonics are limited by the spectrometer's slit in the horizontal direction. In the meantime, the XUV spectrometer records any variations associated with the harmonic beam intensity profile in the vertical direction, as shown in Fig. 7. It is important to note that diffraction effects are not present in this scenario, and the spatial profile remains largely unaffected by the slit along the vertical axis. Moreover, this does not result in diffracted harmonics appearing after passing through the grating.

In the next step [Fig. 7(c)], the positions of DOE and BBO crystals were interchanged, as illustrated in Fig. 6(b), while all other experimental conditions remained the same. The structured array beam produced by the DOE corresponds to both input beams, the 800 nm fundamental and the 400 nm second harmonic. As a result, the TCP-induced harmonic enhancement is observed for 10H, along with a weak $4(n + 1)$ harmonic (12H) and two odd harmonics (9H, 11H), confirming the weak interaction of second harmonic and fundamental array laser pulses ($\omega + 2\omega$) in argon. Despite a variation in intensities of other harmonic orders (9H, 11H, and 12H) in the spectrum (see Fig. S2 in the supplementary material), the spatial structure of the high-harmonic beam corresponding to strong 10H that appeared in both experimental arrangements is nearly identical.

The strong 10H observed in both cases comprised bright and dark intensities. Each dark node in the high-harmonic array beam experiences a π-phase jump in the XUV compared to the bright nodes, as illustrated in the intensity distribution and corresponding cross-sectional profiles shown in Figs. 7(b1) and 7(c1). Notably, the change in waveplate angle does not wipe out the intensity at the positions of the bright spots. The $2(2n + 1)$ even-order harmonics, specifically the 10H harmonic with a Gaussian intensity profile along the vertical axis, is depicted in Fig. 7(a), where its full width at half maximum (FWHM) is measured to be 0.88 mm. The structured pattern corresponding to the 10^{th} harmonic is shown in Figs. 7(b1) and 7(c1). For these high-harmonic array beams (10H), the distances between the centers of the brightest spot (mainlobe) and the immediate secondary bright spot in the detected harmonic are measured as 0.34 and 0.38 mm, respectively. However, the distance between the centers of adjacent secondary bright spots in the

10th harmonic array pattern shown in Fig. 7(b1) ranges from 0.17 mm to 0.15 mm. The spots positioned away from the brightest one in the harmonic array beam are closely associated with their adjacent counterparts. Similarly, the distance between the centers of adjacent secondary bright spots in the 10th harmonic array pattern illustrated in Fig. 7(c1) ranges from 0.2 mm to 0.17 mm. These 10th harmonic measurements are compared with the spot pattern of the fundamental or pump array beam spread over one quadrant, where the distance between the centers of the brightest spot (mainlobe) and the immediate secondary bright spot in the pump array beam is measured as 0.41 mm. In addition, the distance between the adjacent bright secondary bright spots in the pump array beam ranges from 0.28 mm to 0.13 mm. The spots that appear farther from the brightest one (mainlobe) are spaced more narrowly. These measurements exclusively elucidate that the generated XUV beam is a structured array beam whose characteristics strongly correlate with the characteristics of the driving laser field.

However, for enhancing high-harmonics with weak intensities (9H, 11H, and 12H), one can employ an achromatic lens that is corrected to bring the second harmonic and fundamental laser pulses to have better focus than could be obtained with a conventional lens. This would improve the interaction between the second harmonic and fundamental array laser pulses in argon, which can be considered for future research. Overall, the present work highlights intense non-perturbative interactions between the structured laser field and gaseous medium that facilitate analyzing the classical and unique spatial features of generated high-harmonics, which could guide future experiments and beckon exploration of new technologies.

IV. CONCLUSION

We have experimentally demonstrated a flexible approach to generate shape-invariant high-harmonic array beams using ultrashort structured array beams in the near-IR as the pump source, whose beam shape remained unchanged in free-space propagation. In addition, we demonstrated the self-healing ability of focused shape-invariant array beams against undesired structure deformation or astigmatic transformation induced by a tilted lens. The shape-invariant array beam has been proven to be insensitive to changes in the polarization state of the input Gaussian beam.

We employed pump array beams to generate high-harmonic radiation in a gas target driven by a two-color laser field generated in a 0.2 mm thick BBO crystal. That led to enhanced high-harmonic intensity, particularly for the 10th harmonic. However, other high harmonics appeared only with weak intensities and barely visible spatial features. Interestingly, independent of the position of the frequency doubling crystal, a strong 10th harmonic preserved a similar spatial structure as the pumping array beams. This effect establishes that spatially structured high-harmonic radiation exhibits shape-invariant features even after a one meter long propagation from the gas jet to the detector, which so far has not been reported.

These high-harmonic array beams have a unique spatial distribution that enables sensitive extreme ultraviolet tools, opening up new avenues in the field of nonlinear optics and inspiring applications. Since the generated array beams are unique and easy to implement in different experiments and applications, one can design a series of efficient diffractive optical elements with diverse phase functions to realize a new class of structured high-harmonic generation with diverse properties, such as orbital angular momentum,[23–25,63,64] propagation-invariant beams,[64] and harmonic combs with tunable spacing.[65] Finally, the present work provides an opportunity to generate array-shaped XUV harmonics via high-harmonic generation in a noble gas, opening new possibilities and instrumental tools in the XUV that are useful in attosecond pulses created by the HHG process,[63] soft x-ray harmonic combs,[65] high-resolution microscopy,[66] diffractive imaging,[67,68] and lithography.[69,70]

SUPPLEMENTARY MATERIAL

Refer to the supplementary material for an analysis of diffraction efficiency and the polarization dependence of the Hitachi reflection grating, including additional details on the experimental results pertaining to high-harmonic generation.

ACKNOWLEDGMENTS

We gratefully acknowledge funding support from Deutsche Forschungsgemeinschaft via Project No. ZA 110/28-1, European Regional Development Fund (Grant No. 1.1.1.5/19/A/003), State Task for Universities (Grant No. FZGU-2023-0007), Horizon 2020 Framework Programme Grant agreement No. 857627 (CIPHR). We are indebted to Matthias Dreimann (Center for Soft Nanoscience (SoN), University of Münster) for calculating the grating efficiency.

AUTHOR DECLARATIONS

Conflict of Interest

The authors have no conflicts to disclose.

Author Contributions

Andra Naresh Kumar Reddy: Conceptualization (lead); Formal analysis (lead); Investigation (lead); Methodology (lead); Resources (lead); Validation (lead); Visualization (lead); Writing – original draft (lead); Writing – review & editing (equal). **Helmut Zacharias**: Formal analysis (equal); Resources (supporting); Validation (supporting); Writing – review & editing (equal). **Hasan Yilmaz**: Investigation (supporting); Writing – review & editing (equal). **Vyacheslav V. Kim**: Investigation (supporting). **Victor Kärcher**: Investigation (supporting). **Vijayakumar Anand**: Investigation (supporting). **Rashid A. Ganeev**: Formal analysis (supporting); Writing – review & editing (equal).

DATA AVAILABILITY

The data and datasets underlying the results presented in this study are available from the corresponding author upon reasonable request.

REFERENCES

[1] Y. Shen, X. Wang, Z. Xie, C. Min, X. Fu, Q. Liu, M. Gong, and X. Yuan, "Optical vortices 30 years on: OAM manipulation from topological charge to multiple singularities," Light: Sci. Appl. **8**, 90 (2019).

[2]A. Forbes, M. de Oliveira, and M. R. Dennis, "Structured light," Nat. Photonics **15**, 253–262 (2021).
[3]D. Liu, C. Zhou, P. Lu, J. Xu, Z. Yue, and S. Teng, "Generation of vector beams with different polarization singularities based on metasurfaces," New J. Phys. **24**, 043022 (2022).
[4]L. Han, S. Liu, P. Li, Y. Zhang, H. Cheng, X. Gan, and J. Zhao, "Managing focal fields of vector beams with multiple polarization singularities," Appl. Opt. **55**, 9049–9053 (2016).
[5]Z. Chen, T. Zeng, B. Qian, and J. Ding, "Complete shaping of optical vector beams," Opt. Express **23**, 17701–17710 (2015).
[6]D. Naidoo, F. Roux, A. Dudley, I. Litvin, B. Piccirillo, L. Marrucci, and A. Forbes, "Controlled generation of higher-order Poincaré sphere beams from a laser," Nat. Photonics **10**, 327–332 (2016).
[7]C. He, Y. Shen, and A. Forbes, "Towards higher-dimensional structured light," Light: Sci. Appl. **11**, 205 (2022).
[8]Y. Ohtake, T. Ando, N. Fukuchi, N. Matsumoto, H. Ito, and T. Hara, "Universal generation of higher-order multiringed Laguerre-Gaussian beams by using a spatial light modulator," Opt. Lett. **32**, 1411–1413 (2007).
[9]N. K. Fontaine, R. Ryf, H. Chen, D. T. Neilson, K. Kim, and J. Carpenter, "Laguerre-Gaussian mode sorter," Nat. Commun. **10**, 1865 (2019).
[10]N. Jhajj, I. Larkin, E. W. Rosenthal, S. Zahedpour, J. K. Wahlstrand, and H. M. Milchberg, "Spatiotemporal optical vortices," Phys. Rev. X **6**, 031037 (2016).
[11]A. Chong, C. Wan, J. Chen, and Q. Zhan, "Generation of spatiotemporal optical vortices with controllable transverse orbital angular momentum," Nat. Photonics **14**, 350–354 (2020).
[12]C. Wan, A. Chong, and Q. Zhan, "Optical spatiotemporal vortices," eLight **3**, 11 (2023).
[13]F. Feng and X. Yuan, "A new member of the structured light family: Optical spatiotemporal vortices," Light: Sci. Appl. **12**, 236 (2023).
[14]A. E. Willner, H. Huang, Y. Yan, Y. Ren, N. Ahmed, G. Xie, C. Bao, L. Li, Y. Cao, Z. Zhao, J. Wang, M. P. J. Lavery, M. Tur, S. Ramachandran, A. F. Molisch, N. Ashrafi, and S. Ashrafi, "Optical communications using orbital angular momentum beams," Adv. Opt. Photonics **7**, 66–106 (2015).
[15]S. Yu, "Potentials and challenges of using orbital angular momentum communications in optical interconnects," Opt. Express **23**, 3075–3087 (2015).
[16]K. Volkesepúlveda, S. Chávezcerda, V. Garcéschávez, and K. Dholakia, "Three-dimensional optical forces and transfer of orbital angular momentum from multiringed light beams to spherical microparticles," J. Opt. Soc. Am. B **21**(10), 1749–1757 (2004).
[17]A. A. Kovalev, V. V. Kotlyar, and A. P. Porfirev, "Optical trapping and moving of microparticles by using asymmetrical Laguerre-Gaussian beams," Opt. Lett. **41**(11), 2426 (2016).
[18]H. S. Chai and L. G. Wang, "Improvement of optical trapping effect by using the focused high-order Laguerre–Gaussian beams," Micron **43**(8), 887–892 (2012).
[19]X. Zhou, Z. Chen, Z. Liu, and J. Pu, "Experimental investigation on optical vortex tweezers for microbubble trapping," Open Phys. **16**(1), 383–386 (2018).
[20]Z. Li, O. Allegre, and L. Li, "Realising high aspect ratio 10 nm feature size in laser materials processing in air at 800 nm wavelength in the far-field by creating a high purity longitudinal light field at focus," Light: Sci. Appl. **11**, 339 (2022).
[21]R. Drevinskas, J. Zhang, M. Beresna, M. Gecevičius, A. G. Kazanskii, Y. P. Svirko, and P. G. Kazansky, "Laser material processing with tightly focused cylindrical vector beams," Appl. Phys. Lett. **108**(22), 221107 (2016).
[22]J. Ni, C. Wang, C. Zhang, Y. Hu, L. Yang, Z. Lao, B. Xu, J. Li, D. Wu, and J. Chu, "Three-dimensional chiral microstructures fabricated by structured optical vortices in isotropic material," Light: Sci. Appl. **6**, e17011 (2017).
[23]C. Hernández-García, A. Turpin, J. San Román, A. Picón, R. Drevinskas, A. Cerkauskaite, P. G. Kazansky, C. G. Durfee, and I. J. Sola, "Extreme ultraviolet vector beams driven by infrared lasers," Optica **4**, 520–526 (2017).
[24]Y. Hu, Z. Ye, H. Li, C. Lu, F. Chen, J. Wang, S. Pan, M. Zhang, J. Gao, and J. Wu, "Generation of vortex N_2^+ lasing," Optica **10**, 682–687 (2023).
[25]V. Kärcher, V. V. Kim, A. N. K. Reddy, H. Zacharias, and R. A. Ganeev, "Generation of complex vector and vortex extreme ultraviolet beams using the S-waveplate and spiral phase plate during high-order harmonics generation in argon," ACS Photonics **10**(12), 4519–4528 (2023).
[26]F. Courvoisier, *Nonstandard Light for Ultrafast Laser Microstructuring and Nanostructuring*, 239 (Springer, Cham, 2023), pp. 581–621.
[27]M. Sakakura, Y. Lei, L. Wang, Y. H. Yu, and P. G. Kazansky, "Ultralow-loss geometric phase and polarization shaping by ultrafast laser writing in silica glass," Light: Sci. Appl. **9**, 15 (2020).
[28]A. P. Ignatius Xavier, F. G. Arockiaraj, S. Gopinath, A. S. John Francis Rajeswary, A. N. K. Reddy, R. A. Ganeev, M. S. A. Singh, S. D. M. V. Tania, and V. Anand, "Single-shot 3D incoherent imaging using deterministic and random optical fields with Lucy–Richardson–Rosen algorithm," Photonics **10**, 987 (2023).
[29]F. Barrows, A. K. Petford-Long, and C. Phatak, "3D magnetic imaging using electron vortex beam microscopy," Commun. Phys. **5**, 324 (2022).
[30]G. A. Siviloglou, J. Broky, A. Dogariu, and D. N. Christodoulides, "Observation of accelerating Airy beams," Phys. Rev. Lett. **99**, 213901 (2007).
[31]Z. Zheng, B.-F. Zhang, H. Chen, J. Ding, and H.-T. Wang, "Optical trapping with focused Airy beams," Appl. Opt. **50**, 43–49 (2011).
[32]M. Chen, S. Huang, X. Liu, Y. Chen, and W. Shao, "Optical trapping and rotating of micro-particles using the circular Airy vortex beams," Appl. Phys. B **125**, 184 (2019).
[33]J. Durnin, J. J. Miceli, and J. H. Eberly, "Diffraction-free beams," Phys. Rev. Lett. **58**, 1499–1501 (1987).
[34]J. Dudutis, P. Gečys, and G. Račiukaitis, "Non-ideal axicon-generated Bessel beam application for intra-volume glass modification," Opt. Express **24**, 28433–28443 (2016).
[35]J. Dudutis, R. Stonys, G. Račiukaitis, and P. Gečys, "Glass dicing with elliptical Bessel beam," Opt Laser. Technol. **111**, 331–337 (2019).
[36]D. McGloin, V. Garcés-Chávez, and K. Dholakia, "Interfering Bessel beams for optical micromanipulation," Opt. Lett. **28**, 657–659 (2003).
[37]L. Gao, L. Shao, B.-C. Chen, and E. Betzig, "3D live fluorescence imaging of cellular dynamics using Bessel beam plane illumination microscopy," Nat. Protoc. **9**, 1083–1101 (2014).
[38]X. Y. Weng, Q. Song, X. M. Li, X. M. Gao, H. M. Guo, J. L. Qu, and S. L. Zhuang, "Free-space creation of ultralong anti-diffracting beam with multiple energy oscillations adjusted using optical pen," Nat. Commun. **9**, 5035 (2018).
[39]Y. Zhang, H. Chang, X. Chen, Y. An, T. Hou, P. Ma, R. Su, and P. Zhou, "Design and generation of structured array beams with shape-invariant properties," New J. Phys. **25**, 053029 (2023).
[40]A. Forbes, "Structured light from lasers," Laser Photonics Rev. **13**, 1900140 (2019).
[41]P. Slevas, K. Mundrys, O. Ulcinas, and S. Orlov, "An optical needle with elongated transversal profile created using Airy beams for laser processing of glasses," Opt Laser. Technol. **174**, 110558 (2024).
[42]B. Kim, S. Choi, S. J. Won, Y. W. Kim, Y.-J. Kim, and S.-W. Kim, "Coherent manipulation of extreme-ultraviolet Bessel Vortex Beams from solids by active wavefront shaping of driving fundamental beams," ACS Photonics **10**, 3458–3466 (2023).
[43]A. Kritzinger, A. Forbes, and P. B. C. Forbes, "Optical trapping and fluorescence control with vectorial structured light," Sci. Rep. **12**, 17690 (2022).
[44]Y. Yang, Y. Ren, M. Chen, Y. Arita, and C. Rosales-Guzmán, "Optical trapping with structured light: A review," Adv. Photonics **3**(03), 034001 (2021).
[45]J. P. Angelo, S.-J. K. Chen, M. Ochoa, U. Sunar, S. Gioux, and X. Intes, "Review of structured light in diffuse optical imaging," J. Biomed. Opt. **24**(07), 071602 (2018).
[46]G.-B. Zhang, X.-Z. Gao, X.-F. Sun, R. Ma, Y. Wang, and Y. Pan, "Airy-Gaussian vector beam and its application in generating flexible optical chains," Opt. Express **31**, 30319–30331 (2023).
[47]L. Wang, X. Ji, X. Li, T. Wang, H. Yu, and Q. Li, "Focusing and self-healing characteristics of Airy array beams propagating in self-focusing media," Appl. Phys. B **125**(9), 165 (2019).
[48]L. Zhou, Y. Jiang, P. Zhang, W. Fan, and X. Li, "Directly writing binary multi-sector phase plates on fused silica using femtosecond laser," High Power Laser Sci. Eng. **6**, e6 (2018).
[49]S. N. Khonina, A. V. Ustinov, S. A. Fomchenkov *et al.*, "Formation of hybrid higher-order cylindrical vector beams using binary multi-sector phase plates," Sci. Rep. **8**, 14320 (2018).

[50]S. D. C. Roscam Abbing, R. Kolkowski, Z.-Y. Zhang, F. Campi, L. Lötgering, A. F. Koenderink, and P. M. Kraus, "Extreme-ultraviolet shaping and imaging by high-harmonic generation from nanostructured silica," Phys. Rev. Lett. **128**, 223902 (2022).
[51]X. Yu, K.-Q. Chen, and Y. Zhang, "Optimization design of diffractive phase elements for beam shaping," Appl. Opt. **50**, 5938–5943 (2011).
[52]V. Dev, A. N. K. Reddy, and V. Pal, "Generation of uniform-intensity light beams with controllable spatial shapes," Opt. Commun. **475**, 126226 (2020).
[53]Z. Qu, S. Sun, J. Wang, M. Jiang, F. Zhang, X. Wang, J. Shao, G. Liang, and P. Wang, "Application of ultrafast laser beam shaping in micro-optical elements," J. Laser Appl. **35**(3), 031202 (2023).
[54]A. N. K. Reddy and V. Pal, "Robust design of diffractive optical elements for forming flat-top beams with extended depth of focus," Appl. Phys. B **125**, 231 (2019).
[55]T. Suwada, M. Satoh, S. Telada, and K. Minoshima, "Experimental investigation on focusing characteristics of a He-Ne laser using circular fresnel zone plate for high-precision alignment of linear accelerators," Rev. Sci. Instrum. **83**(5), 053301 (2012).
[56]V. V. Kotlyar, A. A. Kovalev, and A. P. Porfirev, "Astigmatic transforms of an optical vortex for measurement of its topological charge," Appl. Opt. **56**(14), 4095–4104 (2017).
[57]A. N. K. Reddy, V. V. Kim, V. Kärcher, H. Zacharias, A. Bundulis, A. Sarakovskis, A. Atvars, A. Ubelis, and R. A. Ganeev, "Spatial shaping of low- and high-order harmonics generated using vortex beams," J. Phys. D: Appl. Phys. **57**, 305105 (2024).
[58]I. J. Kim, C. M. Kim, H. T. Kim, G. H. Lee, Y. S. Lee, J. Y. Park, D. J. Cho, and C. H. Nam, "Highly efficient high-harmonic generation in an orthogonally polarized two-color laser field," Phys. Rev. Lett. **94**, 243901 (2005).
[59]Y. Yu, X. Song, Y. Fu, R. Li, Y. Cheng, and Z. Xu, "Theoretical investigation of single attosecond pulse generation in an orthogonally polarized two-color laser field," Opt. Express **16**, 686–694 (2008).
[60]I. J. Kim, G. H. Lee, S. B. Park, Y. S. Lee, T. K. Kim, C. H. Nam, T. Mocek, and K. Jakubczak, "Generation of submicrojoule high harmonics using a long gas jet in a two-color laser field," Appl. Phys. Lett. **92**, 021125 (2008).
[61]K. S. Budil, P. Salieres, A. L'Huillier, T. Ditmire, and M. D. Perry, "Influence of ellipticity on harmonic generation," Phys. Rev. A **48**, R3437 (1993).
[62]A. Säynätjoki, L. Karvonen, H. Rostami *et al.*, "Ultra-strong nonlinear optical processes and trigonal warping in MoS_2 layers," Nat. Commun. **8**, 893 (2017).
[63]C. Hernández-García, A. Picon, J. San Roman, and L. Plaja, "Attosecond extreme ultraviolet vortices from high-order harmonic generation," Phys. Rev. Lett. **111**, 083602 (2013).
[64]A. K. Pandey, A. de las Heras, T. Larrieu, J. San Román, J. Serrano, L. Plaja, E. Baynard, M. Pittman, G. Dovillaire, S. Kazamias, C. Hernández-García, and O. Guilbaud, "Characterization of extreme ultraviolet vortex beams with a very high topological charge," ACS Photonics **9**(3), 944–951 (2022).
[65]L. Rego, N. J. Brooks, Q. L. D. Nguyen, J. S. Román, I. Binnie, L. Plaja, H. C. Kapteyn, M. M. Murnane, and C. Hernández-García, "Necklace-structured high-harmonic generation for low-divergence, soft x-ray harmonic combs with tunable line spacing," Sci. Adv. **8**, eabj7380 (2022).
[66]W. Chao, B. D. Harteneck, J. A. Liddle, E. H. Anderson, and D. T. Attwood, "Soft X-ray microscopy at a spatial resolution better than 15 nm," Nature **435**, 1210–1213 (2005).
[67]J. Miao, T. Ishikawa, I. K. Robinson, and M. M. Murnane, "Beyond crystallography: Diffractive imaging using coherent x-ray light sources," Science **348**, 530–535 (2015).
[68]M. D. Seaberg, B. Zhang, D. F. Gardner, E. R. Shanblatt, M. M. Murnane, H. C. Kapteyn, and D. E. Adams, "Tabletop nanometer extreme ultraviolet imaging in an extended reflection mode using coherent Fresnel ptychography," Optica **1**, 39–44 (2014).
[69]C. Wagner and N. Harned, "Lithography gets extreme," Nat. Photonics **4**, 24–26 (2010).
[70]G. Tallents, E. Wagenaars, and G. Pert, "Lithography at EUV wavelengths," Nat. Photonics **4**, 809–811 (2010).